




Machine Learning-Based Algorithm for SAR Wave Parameters Retrieval During a Tropical Cyclone

Weizeng Shao , *Member, IEEE*, Yuyi Hu, Maurizio Migliaccio , *Fellow, IEEE*, Armando Marino , *Member, IEEE*, and Xingwei Jiang

Abstract—The major objective of our research is to retrieve wave parameters from synthetic aperture radar (SAR) images during a tropical cyclone (TC) based on a machine learning method. In this study, more than 2000 Sentinel-1 images obtained in interferometric-wide and extra wide mode are collected during 200 TCs, which are collocated with hindcasted waves by a third-generation numeric model, namely WAVEWATCH-III (WW3). It is found that wave parameters, i.e., significant wave height (SWH), mean wave period (MWP), and mean wave length (MWL), are correlated with several SAR-measured image variables. Based on these findings, a machine learning method, namely eXtreme Gradient Boosting (XGBoost), is developed through the training dataset using 1600 images. The trained algorithm is tested over 400 images and the retrievals are compared with WW3 simulations. The statistical analysis shows that the root mean squared error (RMSE) and scatter index (SI) of SWH are 0.19 m and 0.06, respectively. The RMSE and SI of MWP are 0.19 s and 0.03, respectively. The RMSE of the MWL is 3.77 m and the SI is 0.04. Comparisons between inverted SWH by XGBoost methods and the altimeter measurements presents a 0.59 m RMSE of SWH with and 0.19 SI. This result is improved comparing to the results (i.e., a 1.44 m RMSE of SWH with a 0.45 SI) achieved by a previous algorithm. Collectively, it is considered that machine learning is a valuable method to extract wave parameters from dual-polarization SAR images.

Index Terms—Machine learning, synthetic aperture radar (SAR), tropical cyclone, wave parameter.

I. INTRODUCTION

TROPICAL cyclones (TCs) associated with heavy rain are a typical disaster in coastal waters and play a crucial role in

Manuscript received 7 February 2024; accepted 13 August 2024. Date of publication 16 August 2024; date of current version 5 September 2024. This work was supported in part by the National Natural Science Foundation of China under Grant 42076238 and Grant 42376174, and in part by the Natural Science Foundation of Shanghai under Grant 23ZR1426900. (*Corresponding author: Weizeng Shao.*)

Weizeng Shao is with the College of Oceanography and Ecological Science, Shanghai Ocean University, Shanghai 201308, China, and also with National Satellite Ocean Application Service, Shanghai 201306, China (e-mail: wzshao@shou.edu.cn).

Yuyi Hu is with the College of Oceanography and Ecological Science, Shanghai Ocean University, Shanghai 201308, China (e-mail: yy-hu@shou.edu.cn).

Maurizio Migliaccio is with the Dipartimento di Ingegneria, Università degli Studi di Napoli “Parthenope,” 80133 Napoli, Italy (e-mail: maurizio.migliaccio@uniparthenope.it).

Armando Marino is with the Earth Observation, Biological and Environmental Sciences, University of Stirling, FK9 4LA Stirling, U.K. (e-mail: armando.marino@stir.ac.uk).

Xingwei Jiang is with National Satellite Ocean Application Service, Beijing 100081, China (e-mail: xwjiang@mail.nsoas.org.cn).

Digital Object Identifier 10.1109/JSTARS.2024.3445129

the momentum and heat exchange at the sea–air interface. Due to the extreme state, it is difficult to measure the TC dynamics by the on-scene technique such as National Data Buoy Center (NDBC) buoy [1]. Since 1980s, ocean numerical models based on theory of oceanography and computing technology have been developed. Based on the theory of third-generation wave model [2], two numeric models, i.e., WAVEWATCH-III (WW3) [3] and simulation wave nearshore [4], have capability for hindcasting wave over global ocean and polar region [5]. The accuracy of hindcasting wave by numeric models relies on the forcing field, however, the underestimation of wind speeds obtained from meteorological numerical models [i.e., European Centre for Medium-Range Weather Forecasts (ECMWF)] in TCs [6] leads to distortion of wave simulations.

Remote sensing is a mature technology for earth surface observation with a wide spatial coverage. At present, the products of upper oceanic dynamics are operationally released over global seas, i.e., sea surface wind from scatterometer [7] and polarimetric microwave radiometer and sea surface wave from altimeter and wave spectrometer (surface waves investigation and monitoring, SWIM) [8]. The scatterometer-measured wind has a coarse spatial resolution (~ 12.5 km) and the spatial resolution of SWIM-measured wave is 18 km. Synthetic aperture radar (SAR) can capture upper ocean dynamics and maritime targets with a finer spatial resolution, i.e., a 10 and 40 m pixels for Sentinel-1 (S-1) in interferometric wide (IW) and extra wide (EW) mode [9], [10]. According to backscattering theory, sea surface roughness affects the radar returns represented by normalized cross section (NRCS) [11]. This was confirmed through the very first experiment of the Seasat mission, where co-polarization [vertical–vertical (VV) and horizontal–horizontal] NRCS were correlated with a wind vector [12]. Following this rationale, a geophysical model function (GMF) initially tailed for scatterometer, can be used for C-band SAR wind retrieval, called CMOD family, i.e., CMOD5N [13] and its latest version CMOD7 [14]. Recently, copolarized GMFs are retuned through abundant SAR measurements [15], [16]. The limitation of copolarized GMFs is the saturation problem of backscattering signals at strong wind (>25 m/s) [17]. In contrast, NRCS in cross-polarization [vertical–horizontal (VH) and horizontal–vertical] suffers no saturation at wind speed up to 55 m/s [18] and is dependent on wind direction [19], [20], meaning that TC wind can be practically retrieved by cross-polarized GMF [21]. A TC wind inversion algorithm is proposed by using dual-polarized (VV and VH) SAR measurements [22]. Taking advantage of this

algorithm, the French Research Institute for Exploitation of the Sea (IFREMER) actually releases a CyclObs wind product based on dual-polarized S-1 image during a TC. Additionally, several algorithms based on azimuthal cutoff wave length are applicable for retrieving TC wind speed from C-band [23] and X-band SAR [24].

It is well recognized that the mechanism of sea surface wave mapping on SAR image consists of tilt [25], hydrodynamic modulation [26], and velocity bunching [27], [28]. Based on this principle, the theoretical SAR wave retrieval algorithms are developed, i.e., the Max Planck Institute algorithm [29], the semi-parametric retrieval algorithm [30], partition rescaling and shift algorithm [31], and the parameterized first-guess spectrum method (PFSM) [32]. These methods based on the first-guess wave spectrum from numeric models or parametric functions taking auxiliary wind from scatterometer or SAR [33]. Furthermore, as for the SAR wave retrieval in TCs, the traditional MTFs employed in theoretical algorithms do not include any consideration of strong wind-induced nonlinearity [34]. In order to avoid the calculation of complex MTFs, wave parameters are directly retrieved from SAR image by empirical models [35], machine learning [36], [37] and fully polarimetric techniques [38], [39]. Although these models are conveniently implemented with regular sea states, SAR wave retrieval algorithm in TCs necessitates to be further improved so as to achieve effective inversion of wave parameters at extreme and complex sea conditions. Machine learning in satellite oceanography has recently gained a lot of attention in the era of big ocean data. Zheng et al. [40] developed an intelligent model driven by satellite data, successfully forecasting the complex, large-scale ocean phenomenon of tropical instability waves. The groundbreaking work by Zheng et al. has demonstrated the feasibility of using purely satellite data-driven intelligent models to forecast complex ocean phenomena for the first time, highlighting the powerful ability of artificial intelligence in mining ocean satellite data. Machine learning also makes significant advances in other areas of satellite oceanography, including ocean-atmosphere parameter retrieval [41], ocean satellite data repair [42], and detection of ocean phenomena [43]. It can effectively model the intricate rules hidden within ocean data. Thus, we applied it in this article for SAR wave parameter retrieval in TCs.

In this study, the dependences of wave parameters, including significant wave height (SWH), mean wave period (MWP), and mean wave length (MWL) on several variables estimated from SAR intensity are studied through more than 2000 S-1 dual-polarized images under the TC seasons in 2015–2023. Subsequently, machine learning is applied for SAR wave retrieval in TCs. The accuracy is evaluated by comparing the SAR retrievals with the measurements of altimeter and inverted results by previous algorithm PFSM. In particular, the contribution of our work is to solve the inapplicability of the regression problem in previous empirical model (i.e., CWAVE). The rest of this article is as follows. The dataset is introduced in Sections II. Section III gives the methodology of machine learning-based wave inversion algorithm; validation and discussion are given in Sections IV and V, respectively; and Section VI concludes this article.

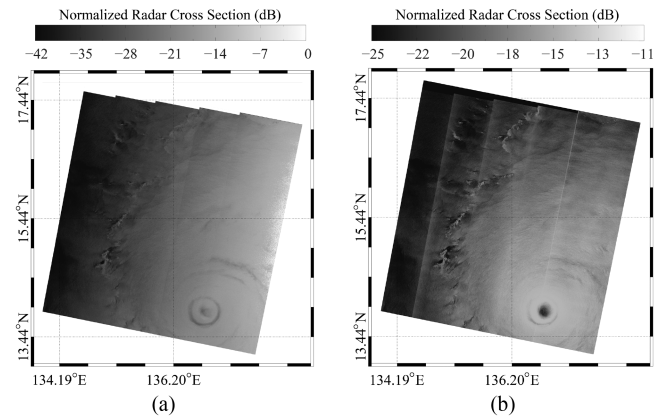


Fig. 1. Normalized radar cross section (NRCS) map relevant to the sentinel-1 (S-1) synthetic aperture radar (SAR) image under tropical cyclone (TC) mangkhut at 20:48 UCT on 11 September 2018. (a) Vertical-vertical (VV). (b) Vertical-horizontal (VH) polarization.

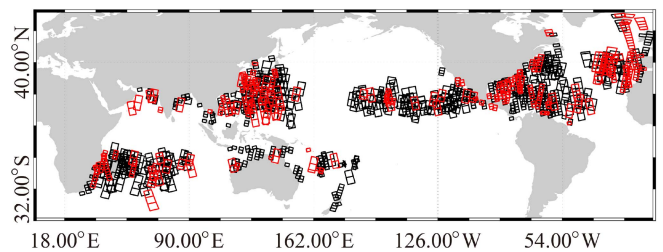


Fig. 2. Geographic locations of the assembled S-1 SAR images during tropical cyclones (TCs) in 2015–2023, in which the black and red boxes are the locations of S-1 images in the training and validation datasets, respectively.

II. DESCRIPTION OF DATASET

In this section, the collected S-1 images and operational CyclObs wind products provided by IFREMER are presented. Besides, corresponding wave fields hindcasted by WW3 model and validation sources, i.e., the available measurements following the footprints of Jason-2 altimeter and NDBC buoys, are described.

A. SAR Image and CyclObs Wind Products

Totally, more than 2000 dual-polarized (VV and VH) S-1 images obtained in IW and EW mode are available for this study. These images are taken during 200 TCs and the distance between geographic locations and TC eyes are within 500 km. The pixel sizes of GRD IW and EW images are 10 and 40 m respectively, incidence angle ranges from 19° to 47° and swath coverage is more than 200 km. In order to enhance the usability of SAR data, calibrated image is denoised by noise-equivalent sigma zero and then is smoothed by a Gaussian filter with a 3×3 pixel. As an example, the VV-polarized and VH-polarized images over TC Mangkhut at 20:48 UCT on 11 September 2018, are exhibited in Fig. 1(a) and (b), respectively. Fig. 2 shows the positions of the S-1 images, where the red and black rectangles correspond to 1600 images in the training dataset and more than 400 images in the test dataset, respectively. Presently, IFREMER

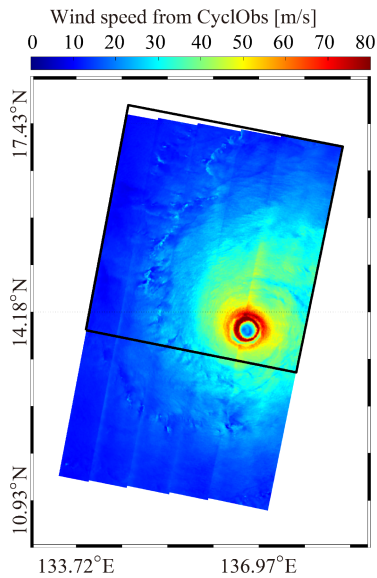


Fig. 3. Wind speed map from CyclObs wind product provided by French research institute for exploitation of the oceans (IFREMER) team and the black boxes represent the location of image in Fig. 1.

officially released the CyclObs wind products derived from dual-polarize S-1 image in TCs. Fig. 3 illustrates the CyclObs wind map relative to the image in Fig. 1. In this case, the cyclonic pattern is clearly visible and the maximum wind speed reaches 80 m/s. Here, CyclObs winds are used as prior information in the application of theoretical-based algorithm PFSM for SAR wave inversion.

B. Hindcasted Wave

Due to the difficulty of obtaining real-time observations with wide spatial coverage in TCs, the hindcasted waves of the third-generation numerical wave model WW3 (version 6.07) developed by the National Oceanic and Atmospheric Administration (NOAA) of the U.S. were aligned with the collected images. Since 1979, ECMWF continuously releases open-access atmospheric-oceanic data, however, ECMWF wind field has significantly underestimation in TCs. In our previous study [44], a composite wind profile at a grid of 0.125° with a 6-h interval, hereafter called H-E, is treated as forcing field in WW3, which combines ECMWF reanalysis (ERA-5) and simulations from parametric Holland model [45] (i.e., the TC shape B of 0.4) taking the TC information from NOAA. Fig. 4 shows the H-E wind map over TC Haishen at 21:00 UCT on 4 September 2020. It has been revealed in recent work [46], that the sea surface current and sea level has nonnegligible effect on the WW3 wave simulation due to strong wave-current interactions in TCs. Therefore, daily sea surface current and sea level from Copernicus marine environment monitoring service (CMEMS) at a grid of 0.08° are also the forcing fields as well as the water depth from general bathymetry chart of the oceans. The CMEMS sea surface current and sea level map over TC Haishen at 21:00 UCT on 4 September 2020 is exhibited in Fig. 5(a) and (b), respectively. The outputs include three wave parameters with a

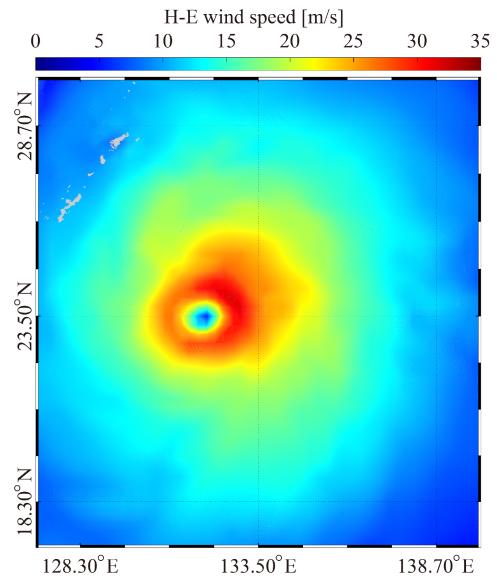


Fig. 4. Wind map composed by 0.25° gridded European centre for medium-range weather forecasts (ECMWF) and parametric holland model, which is taken over tropical cyclone (TC) Haishen.

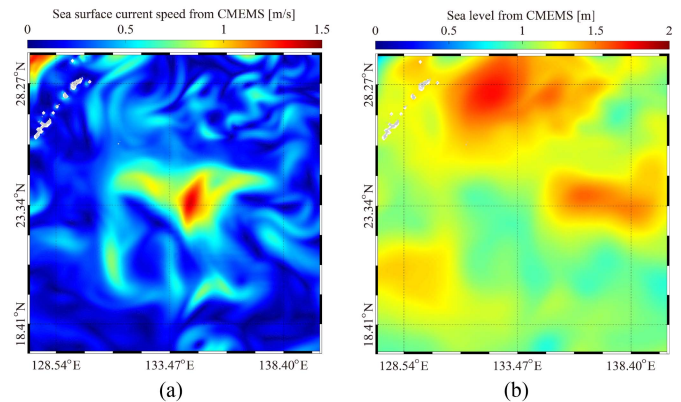


Fig. 5. Daily data map composed by 0.08° gridded from the Copernicus marine environment monitoring service (CMEMS), which is taken at 21:00 UCT on 4 September 2020. (a) Sea surface current. (b) Sea level.

0.05° grid spatial resolution and 30 min temporal resolution, i.e., SWH, MWP, and MWL, which are useful to study the dependences on the variables from SAR images in the training dataset.

C. Altimeter Data and NDBC Buoys

It is rare to obtain the real-time observation from moored buoys in TCs due to extreme sea state. Instead, we used NDBC buoy measurements in the Pacific Ocean between June and October 2021 to assess the accuracy of the WW3 simulations. The WW3-simulated SWH overlaid the positions of collected NDBC buoys and the footprints of altimeter Jason-2 at 21:00 UCT on 11 September 2018 is shown in Fig. 6, in which the black box is the location of the image in Fig. 1 and the red triangle represents the geographic locations of NDBC buoys. Comparing

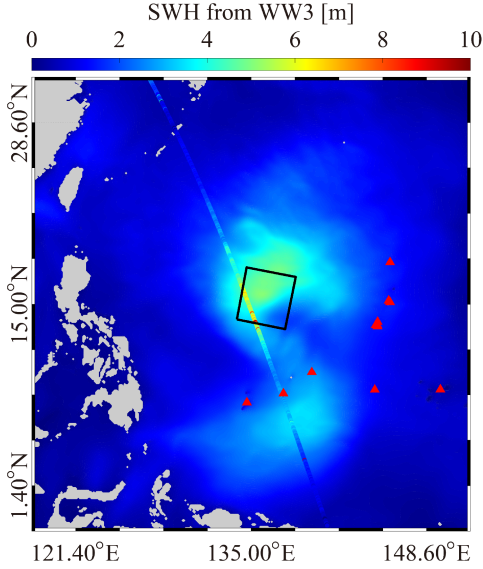


Fig. 6. Simulated wave graph from WAVEWATCH-III (WW3) overlaid by the footprint of the Jason-2 altimeter at 21:00 UCT on 11 September 2018, in which the black rectangle is the location of the image in Fig. 1 and the red triangle represents the collected NDBC buoys geographical situation.

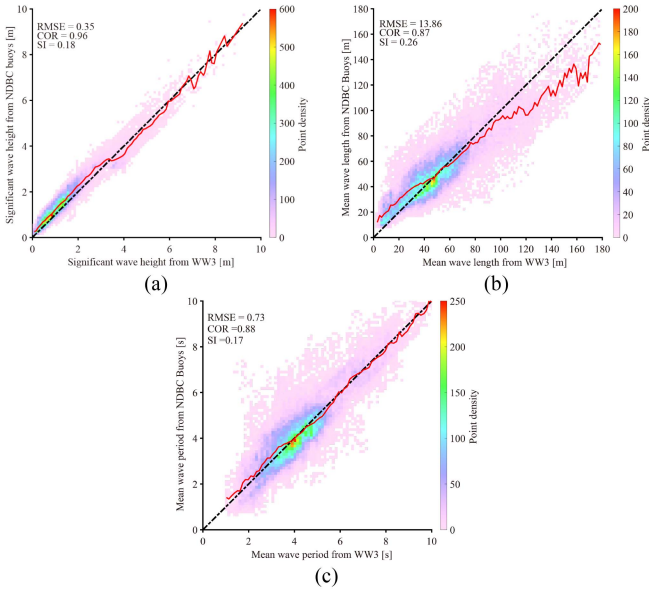


Fig. 7. Comparisons between buoys measurement and collocated WW3-simulations. (a) Significant wave height. (b) Mean wave length. (c) Mean wave period. The full line is the mid-value from WW3 estimations.

the WW3-simulated SWH with the NDBC buoy measurements, the root mean square error (RMSE) of SWH was 0.35 m, the correlation (COR) was 0.96, and the scattering index (SI) was 0.18, as shown in Fig. 7(a). Similarly, the statistical analysis of WW3-simulated MWL and MWP are shown in Fig. 7(b) and (c), respectively, indicating a 13.86 m RMSE with a 0.87 COR and a 0.26 SI for MWL and a 0.73 s RMSE with a 0.88 COR and a 0.17 SI for MWP. Table I lists the comprehensive evaluation results for the WW3 simulation under different sea

TABLE I
COMPARISON BETWEEN SIMULATIONS FROM WW3 AND MEASUREMENTS FROM NDBC BUOYS

Wave Parameters	Sea States	Sample Number	Evaluation Metrics		
			Bias	RMSE	COR
SWH	0–1.5 m	32675	-0.2076	0.3060	0.8660
	1.5m–3 m	11330	-0.2572	0.3927	0.8040
	3m–4.5 m	3537	0.1636	0.4605	0.7535
	>4.5 m	1087	0.1906	0.4938	0.8828
	Total	48633	-0.1835	0.3481	0.9626
MWL	0–1.5 m	32675	-3.4328	13.4549	0.8023
	1.5m–3 m	11330	4.2235	12.7728	0.8213
	3m–4.5 m	3537	3.1116	18.2957	0.7229
	>4.5 m	1087	5.5637	18.8468	0.7291
	Total	48633	-0.9622	13.8560	0.8738
MWP	0–1.5 m	32675	-0.1365	0.7856	0.7454
	1.5m–3 m	11330	0.2324	0.5808	0.8180
	3m–4.5 m	3537	-0.1052	0.6744	0.7372
	>4.5 m	1087	0.0334	0.5775	0.7721
	Total	48633	-0.0445	0.7344	0.8832

state. It is worth noting that most total dataset is at low sea state (0–1.5 m), exhibiting the superior statistical results for three wave parameters. Although the relatively high RMSE of SWH, MWL and MWP was shown in high sea state (>4.5 m), the entire dataset under different sea state condition demonstrates satisfactory results. These results from scatter plot and table confirm the robustness of the WW3-simulated wave. As a matter of fact, products from altimeters are useful for analysis of wave distribution over global seas. In our work, both WW3 simulation and SWH from altimeter Jason-2/3 and Haiyang-2 (HY-2) collocated with the images in the validation dataset are used to discuss the applicability of machine learning-based algorithm.

III. METHODOLOGY

The dependence of wave parameters on variables estimated from SAR intensity are studied and then the derivation of machine learning-based SAR wave retrieval algorithm is described. In addition, the existing algorithm PFSM is briefly introduced.

A. Dependence of Wave Parameters on SAR-Measured Variables

The SAR intensities of the two polarization channels are converted to NRCS, and then the calibrated image is divided into several subscenes at a distance of 3–5 km in the range×azimuth direction, i.e., 256×256 pixel for IW and 128×128 pixel for EW. The SAR two-dimensional (2-D) spectrum is obtained by performing 2-D Fourier transform on the subscene. As examples, Fig. 8(a) shows the quick-look of a subscene obtained from the image in Fig. 1(a) and the matching 2-D spectrum is displayed in Fig. 8(b). In the literature, the velocity bunching is represented by azimuthal cutoff wavelength λ_c , which is practically estimated by minimizing the standard error of a Gaussian function $G(k_x)$ fitted to the 1-D spectrum integrated in the wave number along look direction k_x , as expressed by the following:

$$G(k_x) = \exp \left\{ -\pi \left(\frac{k_x}{k_c} \right)^2 \right\} \quad (1)$$

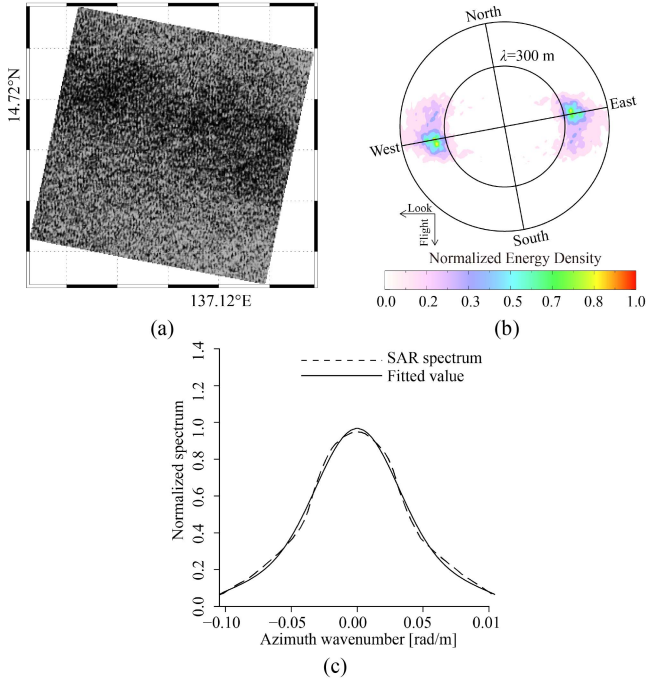


Fig. 8. (a) Subscene obtained from the VV-polarized SAR imagery in Fig. 1(a). (b) SAR two-dimensional spectrum. (c) Gaussian fitted results through the spectrum.

where

$$k_c = \frac{2\pi}{\lambda_c}. \quad (2)$$

As concluded in recent study [28], the azimuthal cutoff wavelength λ_c is independent of polarization, therefore, the VV-polarized λ_c is calculated here. The Gaussian fitted results through the spectrum in Fig. 8(b) are illustrated in Fig. 8(c). In addition, the homogeneity of image *cvar* that is commonly used in empirical CWAVE family is defined as follows:

$$cvar = \text{var} \left(\frac{I - \bar{I}}{\bar{I}} \right) \quad (3)$$

in which I represents the SAR NRCS on subscene and \bar{I} is the average value of I .

The SAR subscenes located at WW3 grids are grouped, in which the time difference between the WW3 simulations and SAR imaging time is less than 15 min. Overall, six parameters are calculated from the subscenes, i.e., VV-polarized σ_0^{VV} , VH-polarized NRCS σ_0^{VH} , VV-polarized cutoff wavelength λ_c normalized by β , *cvar*, Total SAR spectral and wavelength of the SAR image spectrum versus a given range λ . The WW3-simulation collected more than 160 000 samples as a training dataset. Fig. 9 shows the relationships among the SWHs and six parameters, i.e., (a) σ_0^{VV} , (b) σ_0^{VH} , (c) *cvar*, (d) λ_c/β , (e) Total SAR spectral, and (f) λ . Similarly, the relations analysis of WW3-simulated MWP and MWL are shown in Figs. 10 and 11. It was found that SWH, MWL, and MWP are linearly related to σ_0^{VV} , σ_0^{VH} , λ_c/β and Total SAR spectral. The COR value of those parameters is great than 0.3. Furthermore, when λ is less

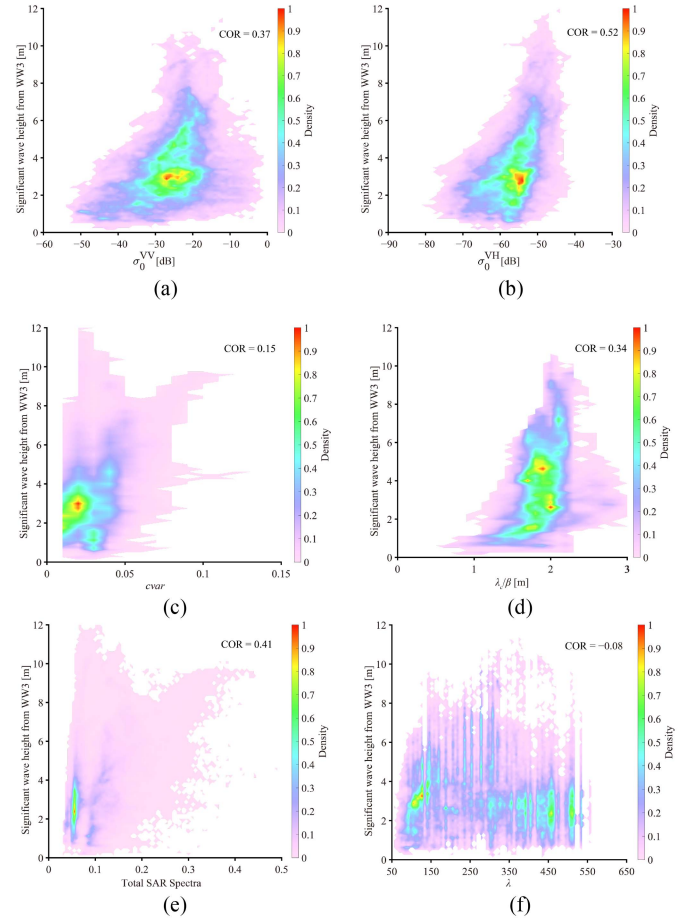


Fig. 9. WW3-simulated SWH versus six parameters. (a) VV-polarized σ_0^{VV} . (b) VH-polarized NRCS σ_0^{VH} . (c) VV-polarized cutoff wavelength λ_c normalized by β . (d) *cvar*. (e) Total SAR spectral. (f) Wavelength of the SAR image spectrum relative to a given range λ .

than 150 m, it is found that there is a certain relationship between the SAR wavelength and the three wave parameters.

B. Derivation of SAR Wave Retrieval Algorithm by Machine Learning

The eXtreme Gradient Boosting (XGBoost) is a powerful machine learning model. The advantage of this method is attributed to its highly optimized algorithms, scalability, and superior performance in a variety of tasks. The core idea of XGBoost is to build a powerful integrated model by training a collection of multiple weak learners (usually decision trees), with each iterative step attempting to correct the errors of the previous model, and each time adding a weak learner (usually a decision tree) to further improve the model's performance. The following is a detailed introduction to the model.

The goal of XGBoost is to minimize the objective function, which was composed of a loss function and a regularization term. It is usually expressed as follows:

$$\text{Obj}(\Theta) = \sum_{i=1}^n \text{Loss}(y_i, \hat{y}_i) + \sum_{k=1}^K \Omega(f_k) \quad (4)$$

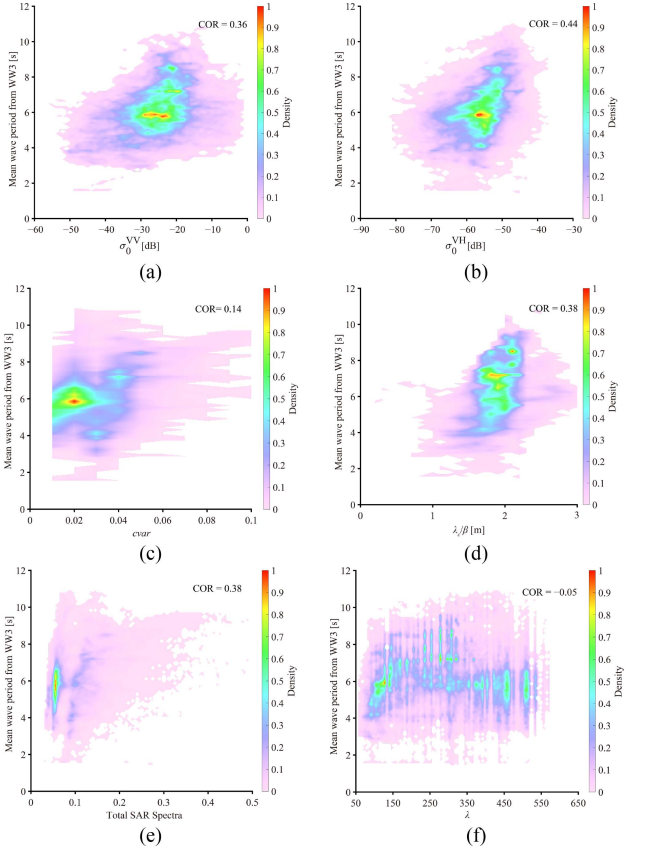


Fig. 10. WW3-simulated MWP versus six parameters. (a) VV-polarized σ_0^{VV} . (b) VH-polarized NRCS σ_0^{VH} . (c) VV-polarized cutoff wavelength λ_c normalized by β . (d) *cvar*. (e) Total SAR spectral. (f) Wavelength of the SAR image spectrum relative to a given range λ .

wherein $\text{Obj}(\Theta)$ represents the objective function of the entire model, Θ including all tree parameters, n represents the number of training samples. $\text{Loss}(y_i, \hat{y}_i)$ is a loss function that calculates the error between the model's predictive value y_i and the actual value \hat{y}_i . K is the number of trees and $\Omega(f_k)$ is the regularization term used to adjust the model complexity.

In order to avoid overfitting, two regularization terms named L1 regularization (Lasso) and L2 regularization (Ridge) were used. The Lasso was used for feature selection and the Ridge was used to control the size of model parameters. The specific formula is shown as follows:

L1 regularization terms:

$$\Omega(f) = \gamma |T| + \frac{1}{2} \sum_{j=1}^{|T|} w_j. \quad (5)$$

L2 regularization term:

$$\Omega(f) = \gamma |T| + \frac{1}{2} \sum_{j=1}^{|T|} w_j^2 \quad (6)$$

wherein T represents the decision tree leaf node, w_j represents the leaf node fraction as the γ represents the regularization term weight.

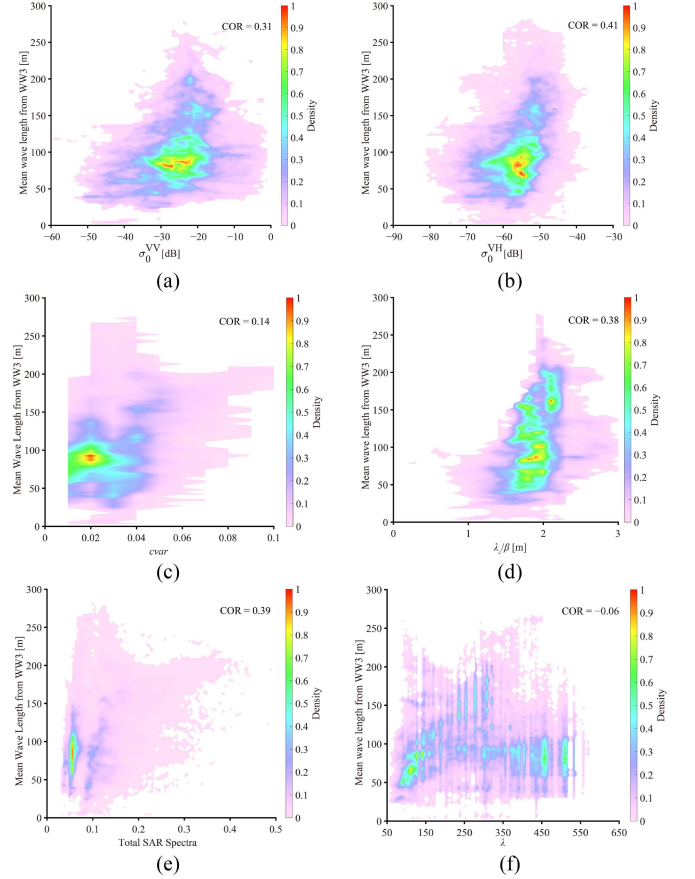


Fig. 11. WW3-simulated MWL versus six parameters. (a) VV-polarized σ_0^{VV} . (b) VH-polarized NRCS σ_0^{VH} . (c) VV-polarized cutoff wavelength λ_c normalized by β . (d) *cvar*. (e) Total SAR spectral. (f) Wavelength of the SAR image spectrum relative to a given range λ .

In general, the XGBoost uses classification and regression trees (CART) decision trees as a base learner. Each CART tree is a binary tree where each node represents a threshold partition of a feature. The model iteratively generates multiple decision trees and comes up with a final prediction by weighted summing their predictions. The XGBoost algorithm flow chart is presented in Fig. 12. In the training process, the input parameters contain the σ_0^{VV} , σ_0^{VH} , λ_c/β , *cvar*, Total SAR spectral, and incidence angle and the output is SWH, MWL, and MWP. The behavior of the XGBoost training process with three wave parameters is illustrated in Fig. 13, i.e., (a) SWH, (b) MWL, and (c) MWP. The results show that the three XGBoost training processes converge eventually, and the RMSE achieved is less than 0.2 m of SWH, 0.5 m of MWL, and 0.12 s of MWP. The SHAP (Shapley Additive exPlanations) is a method of explaining machine learning model predictions and the SHAP value is used to measure the importance of each feature to the model. Fig. 14 show the SHAP values highlighted by the feature value corresponding to the characteristic of input parameter (SWH, MWL, and MWP). It is found that the σ_0^{VH} and azimuth has the greatest impact on XGBoost model, while the β and *cvar* are the least factors. It is reasonable that σ_0^{VH} is sensitive with TC wind and wind determines the sea state. In the other hand, the

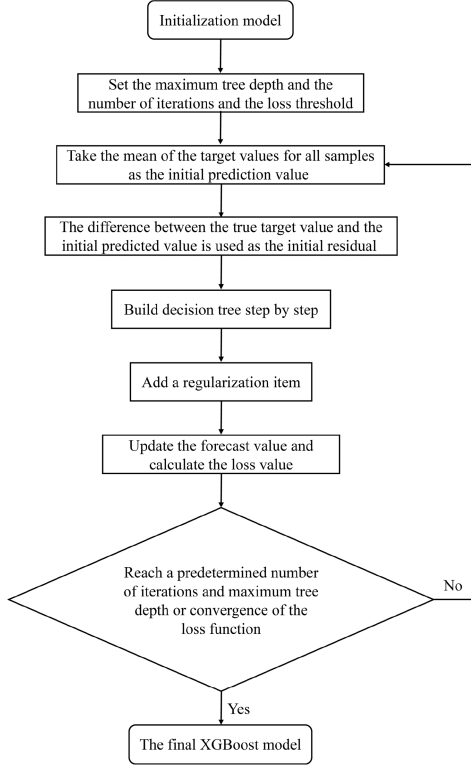


Fig. 12. Flowchart of the eXtreme gradient boosting (XGBoost).

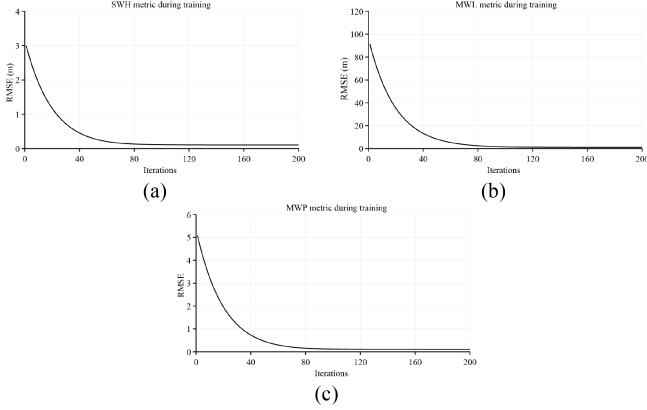


Fig. 13. Behavior of the XGBoost training process. (a) SWH. (b) MWL. (c) MWP.

σ_0^{VV} is most sensitive with backscattering signal. In this sense, the accuracy will be significantly reduces using single-polarized SAR data.

C. Algorithm PFSM

The algorithm PFSM has an advance that is the separation of 2-D SAR spectrum into two portions by (7), i.e., the wind-wave and the swell. The threshold of wave number k_s is expressed by the following:

$$k_s = \left[\frac{2.87gV^2}{R^2U_{10}^4 \cos^2\varphi (\sin^2\varphi \sin^2\theta + \cos^2\varphi)} \right]^{0.33} \quad (7)$$

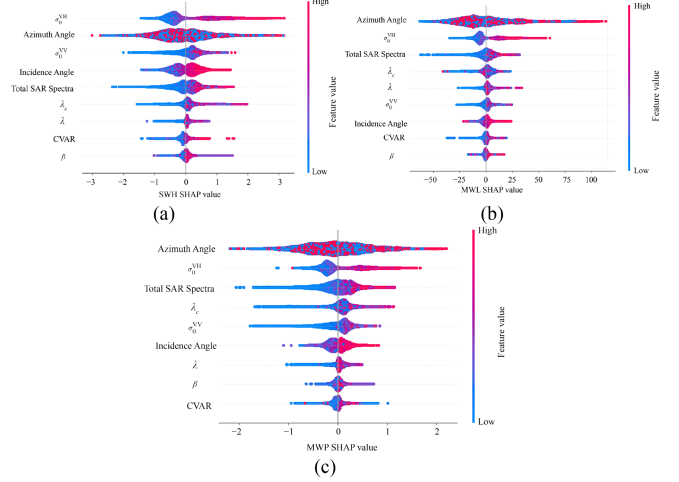


Fig. 14. SHAP value map. (a) SWH. (b) MWL. (c) MWP.

in which g of 9.8 m/s^2 is gravitational acceleration, V represents a flight velocity, R represents the satellite slant range, U_{10} represents the CyclObs wind speed, θ represents the incidence angle, and φ represents the angle of the wave propagation relative to the radar look direction. As for wave number k was larger than k_s , the wind-wave spectrum is inverted by minimizing the cost function J , denoted by the following:

$$J = \int [F_k - \bar{F}_k]^2 dk + \mu \int \left\{ \frac{[E_k - \bar{E}_k]}{[B + \bar{E}_k]} \right\}^2 dk \quad (8)$$

in which F_k represents the retrieved 2-D ocean wave spectrum at wave number k ; \bar{F}_k represents the first-guess spectrum; E_k represents the SAR spectrum; μ represents the weight coefficient; the small positive number B represents supposed to be 0.001 in order to ensure convergence of inversion; and \bar{E}_k represents the mapping SAR spectrum taking the first-guess spectrum estimated by parametric wave function [47] and MTFs as stated in the following [29]:

$$T = 4ik_r \frac{\cot\theta}{1 \pm \sin^2\theta} + 4.5k\omega \frac{i\gamma - \omega}{\omega^2 + i\gamma^2} \sin^2\phi - \frac{R}{V} k_r \omega \left(\cos\theta - i\sin\theta \frac{k_l}{k} \right) \quad (9)$$

wherein T represents the complex MTF consists of three terms: the first term corresponds to the tilt as the function of incidence angle θ and wave number component in azimuth direction k_r ; the second term is the hydrodynamic modulation that is function of wave number k , wave frequency ω , azimuth direction ϕ and attenuation factor γ ; and the nonlinear velocity bunching is illustrated in the final term, in which R represents SAR slant range distance, V represents the flight velocity as well as k_r represents the wave number component in radar look direction. The velocity bunching can be negligible at the region where swell dominate (i.e., $k < k_s$), thus, the swell spectrum can be directly inverted by solving a given part of the SAR spectrum.

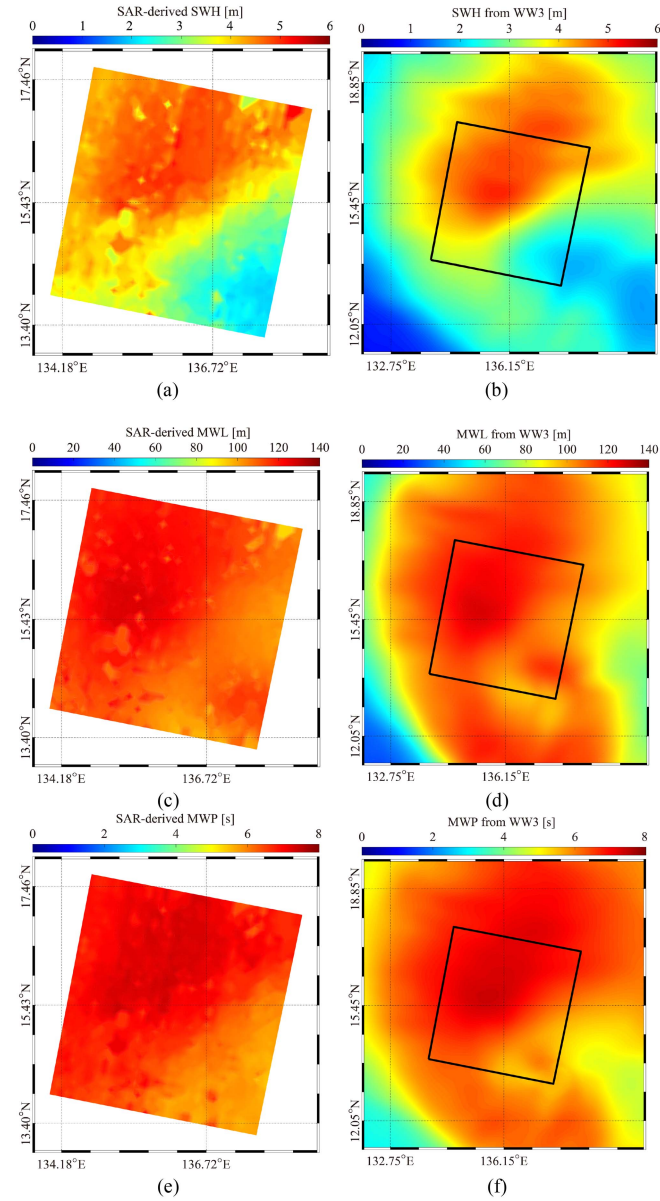


Fig. 15. Inverted wave parameters map from EW images over TC mangkhut at 20:48 UCT on 11 September 2018. (a) SWH. (c) MWL. (e) MWP. The WW3-simulate wave parameters corresponding to SAR image at 21:00 UCT on 11 September 2018. (b) SWH. (d) MWL. (f) MWP.

Ultimately, the synthesized SAR-derived wave spectrum consists of a wind wave spectrum and a swell spectrum. In previous studies, the PFSM algorithm has been applied for wave inversion of a small number of C-band [32] and L-band [33] SAR images. However, the applicability of algorithm PFSM utilizing accurate CyclObs wind necessitates to be confirmed through abundant images acquired in TCs.

IV. RESULTS

In this section, the validations of the machine learning-based approach and the PFSM algorithm against the auxiliary data are presented.

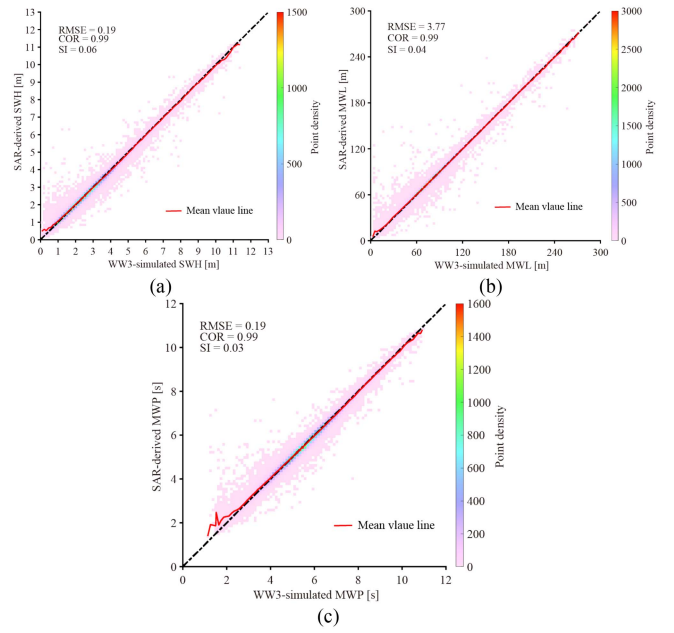


Fig. 16. Comparisons between inverted wave parameters by XGBoost and collocated WW3-simulated wave parameters. (a) SWH. (b) MWL. (c) MWP.

The inverted wave parameters map from EW image over TC Mangkhut at 20:48 UCT on 11 September 2018 by XGBoost was shown in Fig. 15, i.e., (a) SWH, (c) MWL, and (e) MWP. In the meantime, the WW3-simulate wave parameters corresponding to the SAR image at 21:00 UCT on 11 September 2018 was also shown in Fig. 15, i.e., (b) SWH, (d) MWL, and (f) MWP. It was found that the wave parameters derived by XGBoost method have a similar spatial distribution with the WW3-simulated result. Fig. 16 shows the comparisons result between inverted wave parameters (a) SWH, (b) MWL, and (c) MWP by XGBoost with respect to collocated WW3-simulated wave parameters. From the results, it can be seen that the RMSE of SWH is 0.19 m with a 0.99 COR and 0.06 SI [see Fig. 16(a)], a RMSE of MWL is 3.77 m with a 0.99 COR and 0.04 SI [see Fig. 16(b)], and a RMSE of MWP is 0.19 s with a 0.99 COR and 0.03 SI [see Fig. 16(c)]. The red lines shown in Fig. 16 indicate the mid-value of SAR retrievals with a 0.1 m bin of SWH in Fig. 16(a), 1 m bin of MWL in Fig. 16(b) and 0.1s bin of MWP in Fig. 16(c). The results show that XGBoost performs best in medium and high sea situations (SWH > 1 m), and there is an overestimation/underestimation phenomenon in low sea states.

In order to validate the machine learning approach and PFSM against the measurements from altimeters, the comparisons between inverted SWH by two methods with respect to collocated altimeter measurement was conducted in Fig. 17. There were more than 2800 matchups between the SAR and the measurements from three altimeter satellites (Jason-2/3 and HY-2). In the validation, the altimeter measures SWH reached up to 12 m. It is found that RMSE of SWH by the XGBoost method is 0.59 m with a 0.96 correlation (COR) and 0.19 SI [see Fig. 17(a)], which gives better results than the PFSM algorithm with a 1.44 m RMSE, a 0.76 COR and a 0.45 SI [see Fig. 17(b)]. Table II was

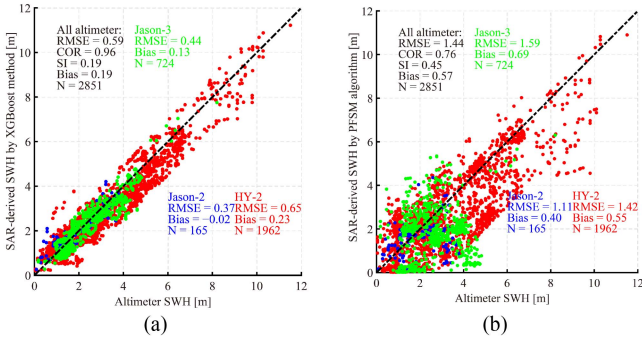


Fig. 17. Comparisons between inverted SWH and collocated altimeter measurements: (a) by XGBoost method and (b) by algorithm PFSM. The altimeter SWH observed from jason-2 (blue), jason-3 (green) and haiyang-2 (HY-2) (red).

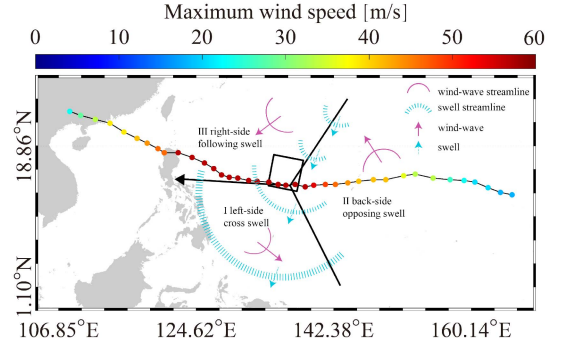


Fig. 18. Wave system in TC mangkhut moving western in the northwest pacific.

TABLE II
COMPARISON BETWEEN WAVE PARAMETERS AND SIMULATIONS FROM WW3

Wave Parameters	Sea States	Sample Numbers	Evaluation Metrics		
			Bias	RMSE	COR
SWH	0–2 m	21972	-0.0556	0.2169	0.8883
	2m–4 m	34671	0.0117	0.1621	0.9556
	4m–6 m	9580	0.0516	0.2173	0.9401
	6m–8 m	3805	0.0383	0.2324	0.9291
	8m–10 m	1591	0.0486	0.2261	0.9344
	>10 m	374	0.108	0.2774	0.8013
Total	71933	-0.00083	0.1941	0.9945	
MWL	0–2 m	21972	-0.4597	5.1746	0.9716
	2m–4 m	34671	0.0869	2.8423	0.9888
	4m–6 m	9580	0.2957	2.9335	0.9943
	6m–8 m	3805	0.1849	3.0909	0.9936
	8m–10 m	1591	0.4411	3.9878	0.986
	>10 m	374	0.7282	5.0623	0.9327
Total	71933	-0.358	3.786	0.9963	
MWP	0–2 m	21972	-0.0448	0.2578	0.9587
	2m–4 m	34671	0.0114	0.142	0.9661
	4m–6 m	9580	0.0379	0.1533	0.9709
	6m–8 m	3805	0.0232	0.146	0.9611
	8m–10 m	1591	0.0319	0.1552	0.9512
	>10 m	374	0.0647	0.149	0.8854
Total	71933	-0.00087	0.1868	0.9923	

conducted to display statistical results under different sea states. It is found that most total dataset is from low and moderate sea states (0–4 m), exhibit the superior statistical results for three wave parameters. Although the lower RMSE of SWH, MWL, and MWP was shown in extreme sea state (>10 m), the entire dataset under four different sea state condition demonstrates satisfactory results in terms of statistical results. Therefore, we consider XGBoost is an optimal machine learning-based algorithm for retrieving TC wave parameters from dual-polarized S-1 image.

V. DISCUSSIONS

As figured out in the previous work [48], the complex wave feature at extreme atmospheric conditions can be divided into three parts, i.e., the right side of the TC motion that is dominated by wind-sea, the left side of the TC motion that is dominated by a mixture of wind-sea and cross swell, and the back of the TC motion that is dominated by counter-swell. To the right of

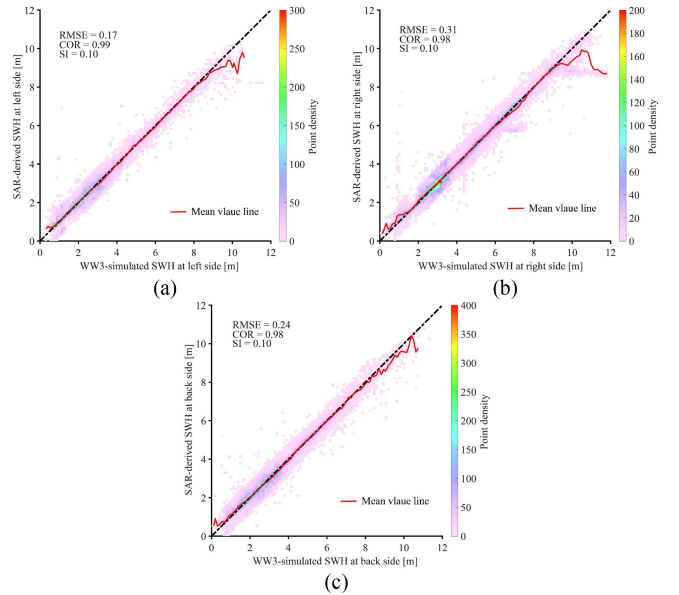


Fig. 19. Comparison of SAR-derived SWHs by the XGBoost method with WW3 model simulations (a) at the left of a TC motion, (b) at the right of a TC motion, and (c) at the back of a TC motion.

the TC motion, the wind-sea dominates under typical strong wind conditions. The wind-sea propagates with surge in the same direction, giving rise to an interaction between the swell and a strong wind-sea energy exchange. Contrarily, to the left of the TC motion, wind-sea and surge propagate vertically, where wind-sea energy is independent of surge energy. At the back side of a TC motion, the wind-sea and surge propagate in opposite directions. Fig. 18 illustrated the wave system in TC Mangkhut moving western in the Northwest Pacific Ocean. Therefore, the precision of the XGBoost method was further investigated for SWH, MWL, and MWP in different parts of the TC motion.

Fig. 19 shows the SWH precision at different parts of the TC motion, i.e., (a) at the left side of a TC motion, (b) at the right side of a TC motion, and (c) at the back side of a typhoon motion. It was found that the RMSE at the left side is 0.17 m with a 0.99 COR and 0.10 SI [see Fig. 19(a)], which has a better performance than the right side of a TC motion, i.e., a 0.31 m RMSE with a 0.98 COR and a 0.10 SI [see Fig. 19(b)] and at the

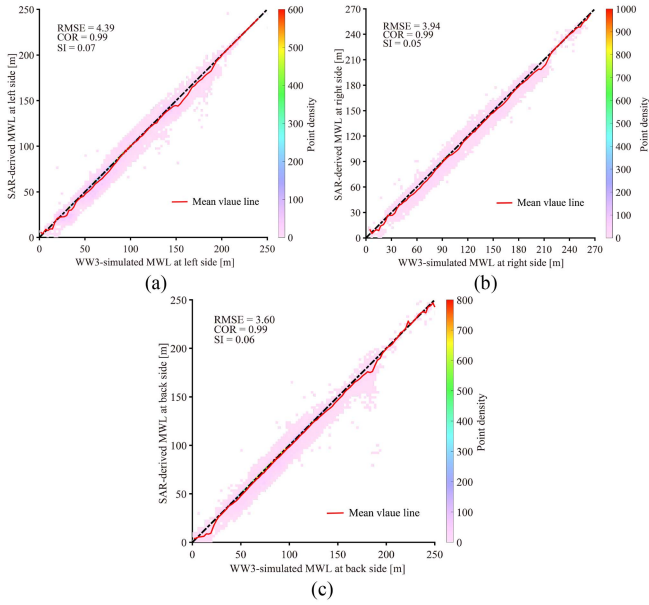


Fig. 20. Comparison of SAR-derived MWL by the XGBoost method and WW3 model simulations (a) at the left of a TC motion, (b) at the right of a TC motion, and (c) at the back of a TC motion.

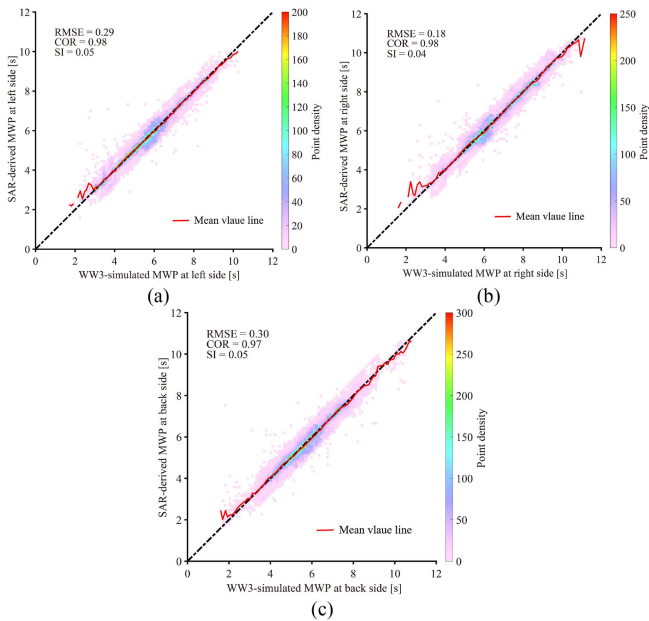


Fig. 21. Comparison of SAR-derived MWP by the XGBoost method and WW3 model simulations (a) at the left of a TC motion, (b) at the right of a TC motion, and (c) at the back of a TC motion.

back side of a TC motion, i.e., a 0.24 m RMSE with a 0.98 COR and a 0.10 SI [see Fig. 19(c)]. The red line in Fig. 19 indicates the median SAR retrieval value for a 0.1 m bin of SWH. It is found that the XGBoost performs the best at the left side of a TC motion. Similarly, the accuracies of MWL and MWP at different sections of typhoon motion were illustrated in Figs. 20 and 21. The statistical result shows that the MWL by XGBoost performs the best at the back position of a TC motion (i.e., a 3.60 m RMSE with a 0.99 COR and a 0.06 SI), while the MWP by XGBoost

performs the best at the right position of a typhoon motion (i.e., a 0.18 s RMSE with a 0.98 COR and a 0.04 SI). Although the accuracy of wave parameters at different parts of TC motions has a certain difference, the machine learning approach has good wave parameters inversion performance for complicated wave characteristics under extreme weather conditions.

VI. CONCLUSION

At present, upper ocean dynamics can be monitoring by several sensors, i.e., sea surface wind from scatterometer and spaceborne polarimetric microwave radiometer and sea surface wave from altimeter and SWIM. However, the spatial resolution of these products (i.e., >10 km) does not satisfy the requirement of complicated air–sea interaction in TCs.

In this article, more than 2000 dual-polarized S-1 images obtained in IW and EW mode during 200 TCs are collected, which are matched with hindcasted wave parameters using WW3 model, in which H-E wind, CMEMS sea surface current and CMEMS sea level are applied as forcing fields. The SWH, MWL, and MWP simulated by WW3 were validated against the measurements of NDBC buoys, and the RMSE of SWH was 0.35 m, COR was 0.96, and SI was 0.18; the RMSE of MWL was 13.86 m, COR was 0.87, and SI was 0.26; and the RMSE of MWP was 0.73 s, COR was 0.88, and SI was 0.17. The difference sea states result show that the entire dataset under four different sea state condition demonstrates satisfactory results in terms of statistical results. It is found that wave parameters, i.e., SWH, MWP, and MWL, are correlated with several SAR-measured image variables (VV-polarized σ_0^{VV} , VH-polarized NRCS σ_0^{VH} , VV-polarized cutoff wavelength λ_c normalized by β , *cvar*, Total SAR spectral, and wavelength of the SAR image spectrum versus a given range λ). Based on these findings, an XGBoost machine learning method is developed through the training dataset from more than 1600 images. The trained algorithm is tested over 400 images and the retrievals are compared with WW3 simulations. Statistical analysis of SWH shows an RMSE of 0.19 m, a COR of 0.99, and a SI of 0.06; MWL shows an RMSE of 3.77 m, a COR of 0.99, and a SI of 0.04; and MWP shows an RMSE of 0.19 s, a COR of 0.99, and a SI of 0.03. Furthermore, a comparison between inverted SWH by XGBoost methods and the algorithm PFSM by the operational CycloObs wind product with respect to collocated altimeter measurements is conducted. The results show that the RMSE for SWH using the XGBoost method is 0.59 m, COR is 0.96, SI is 0.19, which has better performance than that using the PFSM algorithm with a 1.44 m RMSE with a 0.76 COR and a 0.45 SI. Finally, the precision of the XGBoost method for SWH, MWL, and MWP in different sections of the TC motion is given. The statistical result shows that the MWL by XGBoost performs the best at the back side of a cyclone motion (i.e., a 3.60 m RMSE with a 0.99 COR and a 0.06 SI), while the SWH and MWP by XGBoost performs the best at the left position and the right position of a TC motion (i.e., 0.17 m with a 0.99 COR and 0.10 SI and a 0.18 s RMSE with a 0.98 COR and a 0.04 SI). In summary, the machine learning algorithm is a promising approach for wave parameter retrieval in dual-polarized SAR images.

It is revealed that rain and wave breaking has significant influence on the backscattering roughness [49]. In the near future, rain rate and the wave breaking parameter is anticipated to be included in the machine learning algorithm.

ACKNOWLEDGMENT

The authors truly appreciate the free provision of Sentinel-1 images from the European Space Agency via <https://scihub.copernicus.eu> and WAVEWATCH-III by the National Oceanic and Atmospheric Administration via <https://polar.ncep.noaa.gov>. The information of the tropical cyclones is obtained from <https://www.aoml.noaa.gov>. The European Centre for Medium-Range Weather Forecasts (ECMWF) data were obtained from <http://www.ecmwf.int>. The daily sea surface current and sea level are downloaded from Copernicus Marine Environment Monitoring Service via <https://marine.copernicus.eu>. The bathymetric topography from General Bathymetry Chart of the Oceans is gained via <ftp.edcftp.cr.usgs.gov>. The operational products from Jason-2 altimeter are obtained via <https://data.nodc.noaa.gov>. The CyclObs wind production generated by the French Research Institute for Exploitation of the Seas is downloaded via <https://cyclobs.ifremer.fr>.

REFERENCES

- [1] R. C. Beardsley, A. G. Enriquez, C. A. Friehe, and C. A. Alessi, "Intercomparison of aircraft and buoy measurements of wind and wind stress during SMILE," *J. Atmospheric Ocean. Technol.*, vol. 14, no. 4, pp. 969–977, Aug. 1997.
- [2] T. W. Group, "The WAM model—A third generation ocean wave prediction model," *J. Phys. Oceanogr.*, vol. 18, no. 12, pp. 1775–1810, Dec. 1988.
- [3] H. L. Tolman and D. Chalikov, "Source terms in a third-generation wind wave model," *J. Phys. Oceanogr.*, vol. 26, no. 11, pp. 2497–2518, Nov. 1996.
- [4] S. H. Ou, J. M. Liau, T. W. Hsu, and S. Y. Tzang, "Simulating typhoon waves by SWAN wave model in coastal waters of Taiwan," *Ocean Eng.*, vol. 29, no. 8, pp. 947–971, Jul. 2002.
- [5] J. K. Li, L. K. Alison, and H. S. Hayley, "Comparison of wave propagation through ice covers in calm and storm conditions," *Geophys. Res. Lett.*, vol. 42, pp. 5935–5941, Jul. 2015.
- [6] X. H. Li et al., "Tropical cyclone wind field reconstruction and validation using measurements from SFMR and SMAP radiometer," *Remote Sens.*, vol. 14, no. 16, Aug. 2022, Art. no. 3929.
- [7] S. Kako, A. Isobe, and M. Kubota, "High-resolution ASCAT wind vector data set gridded by applying an optimum interpolation method to the global ocean," *J. Geophys. Res. Atmospheres*, vol. 116, no. D23, Dec. 2011, Art. no. D23107.
- [8] G. Z. Liang, J. G. Yang, and J. C. Wang, "Accuracy evaluation of CFOSAT SWIM I2 products based on NDBC buoy and Jason-3 altimeter data," *Remote Sens.*, vol. 13, no. 5, Mar. 2021, Art. no. 887.
- [9] I. Ali, S. Cao, V. Naeimi, C. Paulik, and W. Wagner, "Methods to remove the border noise from Sentinel-1 synthetic aperture radar data: Implications and importance for time-series analysis," *IEEE J. Sel. Topics Appl. Earth Observ. Remote Sens.*, vol. 11, no. 3, pp. 777–786, Mar. 2018.
- [10] A. Pleskachevsky, S. Jacobsen, B. Tings, and E. Schwarz, "Estimation of sea state from Sentinel-1 synthetic aperture radar imagery for maritime situation awareness," *Int. J. Remote Sens.*, vol. 40, no. 11, pp. 4104–4142, May 2019.
- [11] W. R. Alpers, D. B. Ross, and C. L. Rufenach, "On the detectability of ocean surface waves by real and synthetic aperture radar," *J. Geophysical Res., Oceans*, vol. 86, no. C7, pp. 6481–6498, Jul. 1981.
- [12] H. Masuko, K. I. Okamoto, M. Shimada, and S. Niwa, "Measurement of microwave backscattering signatures of the ocean surface using X band and k_a band airborne scatterometers," *J. Geophysical Res., Oceans*, vol. 91, no. C11, pp. 13065–13083, Nov. 1986.
- [13] H. Hersbach, "Comparison of C-band scatterometer CMOD5.N equivalent neutral winds with ECMWF," *J. Atmospheric Ocean. Technol.*, vol. 27, no. 4, pp. 721–736, Apr. 2010.
- [14] A. Stoffelen, J. A. Verspeek, J. Vogelzang, and A. Verhoef, "The CMOD7 geophysical model function for ASCAT and ERS wind retrievals," *IEEE J. Sel. Topics Appl. Earth Observ. Remote Sens.*, vol. 10, no. 5, pp. 2123–2134, May 2017.
- [15] A. A. Mouche and B. Chapron, "Global C-band envisat, RADARSAT-2 and Sentinel-1 SAR measurements in co-polarization and cross-polarization," *J. Geophysical Res., Oceans*, vol. 120, no. 11, pp. 7195–7207, Oct. 2015.
- [16] L. Ren et al., "Assessments of ocean wind retrieval schemes used for Chinese Gaofen-3 synthetic aperture radar co-polarized data," *IEEE Trans. Geosci. Remote Sens.*, vol. 57, no. 9, pp. 7075–7085, Sep. 2019.
- [17] P. A. Hwang and F. Fois, "Surface roughness and breaking wave properties retrieved from polarimetric microwave radar backscattering," *J. Geophysical Res., Oceans*, vol. 120, no. 5, pp. 3640–3657, May 2015.
- [18] B. Zhang and W. Perrie, "Cross-polarized synthetic aperture radar: A new potential measurement technique for hurricanes," *Bull. Amer. Meteorological Soc.*, vol. 93, no. 4, pp. 531–541, Apr. 2012.
- [19] P. W. Vachon and J. Wolfe, "C-band cross-polarization wind speed retrieval," *IEEE Geosci. Remote Sens. Lett.*, vol. 8, no. 3, pp. 456–459, May 2011.
- [20] S. Zhu, W. Z. Shao, A. Marino, J. Sun, and X. Z. Yuan, "Semi-empirical algorithm for wind speed retrieval from Gaofen-3 quad-polarization strip mode SAR data," *J. Ocean Univ. China*, vol. 19, no. 1, pp. 23–35, Feb. 2020.
- [21] H. Shen, W. Perrie, Y. He, and G. Liu, "Wind speed retrieval from VH dual-polarization RADARSAT-2 SAR images," *IEEE Trans. Geosci. Remote Sens.*, vol. 52, no. 9, pp. 5820–5826, Sep. 2014.
- [22] A. A. Mouche, B. Chapron, B. Zhang, and R. Husson, "Combined co-and cross-polarized SAR measurements under extreme wind condition," *IEEE Trans. Geosci. Remote Sens.*, vol. 55, no. 12, pp. 6476–6755, Dec. 2017.
- [23] G. Grieco, W. Lin, M. Migliaccio, F. Nirchio, and M. Portabella, "Dependency of the Sentinel-1 azimuth wavelength cut-off on significant wave height and wind speed," *Int. J. Remote Sens.*, vol. 37, no. 21, pp. 5086–5104, Nov. 2016.
- [24] M. Migliaccio, L. Huang, and A. Buono, "SAR speckle dependence on ocean surface wind field," *IEEE Trans. Geosci. Remote Sens.*, vol. 57, no. 8, pp. 5447–5455, Aug. 2019.
- [25] Y. Zhang, Y. Wang, J. Zhang, and Y. Liu, "Reanalysis of the tilt MTFs based on the C-band empirical geophysical model function," *IEEE Remote Sens. Lett.*, vol. 18, no. 9, pp. 1500–1504, Sep. 2021.
- [26] G. R. Valenzuela, "Theories for the interaction of electromagnetic and oceanic waves—A review," *Boundary-Layer Meteorol.*, vol. 13, pp. 61–85, Feb. 1977.
- [27] W. R. Alpers and C. Bruening, "On the relative importance of motion-related contributions to the SAR imaging mechanism of ocean surface waves," *IEEE Trans. Geosci. Remote Sens.*, vol. GE-24, no. 6, pp. 873–885, Nov. 1986.
- [28] L. Ren, J. S. Yang, X. Dong, Y. J. Jia, and Y. H. Zhang, "Preliminary significant wave height retrieval from interferometric imaging radar altimeter aboard the Chinese Tiangong-2 space laboratory," *Remote Sens.*, vol. 13, no. 12, Jun. 2021, Art. no. 2413.
- [29] K. Hasselmann and S. Hasselmann, "On the nonlinear mapping of an ocean wave spectrum into a synthetic aperture radar image spectrum and its inversion," *J. Geophysical Res., Oceans*, vol. 96, no. C6, pp. 10713–10729, Jun. 1991.
- [30] C. Mastenbroek and C. F. De Valk, "A semiparametric algorithm to retrieve ocean wave spectra from synthetic aperture radar," *J. Geophysical Res., Oceans*, vol. 105, no. C2, pp. 3497–3516, Feb. 2000.
- [31] J. Schulz-Stellenfleth, S. Lehner, and D. Hoja, "A parametric scheme for the retrieval of two-dimensional ocean wave spectra from synthetic aperture radar look cross spectra," *J. Geophysical Res., Oceans*, vol. 110, no. C5, pp. 297–314, May 2005.
- [32] W. Z. Shao, X. W. Jiang, Z. F. Sun, Y. Y. Hu, A. Marino, and Y. G. Zhang, "Evaluation of wave retrieval for Chinese Gaofen-3 synthetic aperture radar," *Geo-spatial Inf. Sci.*, vol. 25, no. 2, pp. 229–243, Apr. 2022.
- [33] Y. Wan, R. Qu, Y. Dai, and X. Zhang, "Research on the applicability of the E spectrum and PM spectrum as the first guess spectrum of SAR wave spectrum inversion," *IEEE Access*, vol. 8, pp. 169082–169095, 2020.
- [34] Y. Y. Hu, W. Z. Shao, X. W. Jiang, W. Zhou, and J. C. Zuo, "Improvement of VV-polarization tilt MTF for Gaofen-3 SAR data of a tropical cyclone," *Remote Sens. Lett.*, vol. 14, no. 5, pp. 461–468, May 2023.

- [35] J. Schulz-Stellenfleth, T. König, and S. Lehner, "An empirical approach for the retrieval of integral ocean wave parameters from synthetic aperture radar data," *J. Geophysical Res., Oceans*, vol. 112, no. C3, Mar. 2007, Art. no. C03019.
- [36] A. Pleskachevsky, B. Tings, S. Wihle, J. Imber, and S. Jacobsen, "Multiparametric sea state fields from synthetic aperture radar for maritime situational awareness," *Remote Sens. Environ.*, vol. 280, Oct. 2022, Art. no. 113200.
- [37] H. Wang et al., "Quad-polarimetric SAR sea state retrieval algorithm from Chinese Gaofen-3 wave mode imagettes via deep learning," *Remote Sens. Environ.*, vol. 273, May 2022, Art. no. 112969.
- [38] B. Zhang, W. Perrie, and Y. J. He, "Validation of RADARSAT-2 fully polarimetric SAR measurements of ocean surface waves," *J. Geophysical Res., Oceans*, vol. 115, no. C6, Jun. 2010, Art. no. C06031.
- [39] W. Z. Shao, Y. Y. Hu, X. W. Jiang, and Y. G. Zhang, "Wave retrieval from quad-polarized Chinese Gaofen-3 SAR image using an improved tilt modulation transfer function," *Geo-Spatial Inf. Sci.*, Jul. 2023.
- [40] G. Zheng, X. F. Li, R. H. Zhang, and B. Liu, "Purely satellite data-driven learning forecast of complicated tropical instability waves," *Sci. Adv.*, vol. 6, no. 29, Jul. 2020, Art. no. eaba1482.
- [41] G. Zheng et al., "Using artificial neural network ensembles with Cropping resampling technique to retrieve sea surface temperature from HY-2A scanning microwave radiometer data," *IEEE Trans. Geosci. Remote Sens.*, vol. 57, no. 2, pp. 985–1000, Feb. 2019.
- [42] G. Zheng and X. Li, "Empirical function method: A precise approach for filling data gaps in satellite sea surface temperature imagery," *IEEE Trans. Geosci. Remote Sens.*, vol. 62, 2024, Art. no. 4200114.
- [43] G. Zheng et al., "Rainband-occurrence probability in Northern Hemisphere tropical cyclones by synthetic aperture radar imagery," *Geophys. Res. Lett.*, vol. 51, no. 10, May 2024, Art. no. e2023GL107555.
- [44] Y. X. Sheng, W. Z. Shao, S. Q. Li, Y. M. Zhang, H. W. Yang, and J. C. Zuo, "Evaluation of typhoon waves simulated by WaveWatch-III model in shallow waters around Zhoushan Islands," *J. Ocean Univ. China*, vol. 18, no. 2, pp. 365–375, Apr. 2019.
- [45] G. J. Holland, "An analytic model of the wind and pressure profiles in hurricanes," *Monthly Weather Rev.*, vol. 108, no. 8, pp. 1212–1218, Dec. 1980.
- [46] H. Cui, H. L. He, X. H. Liu, and Y. Li, "Effect of oceanic current on typhoon-wave modeling in the East China Sea," *Chin. Phys. B.*, vol. 21, no. 10, Oct. 2012, Art. no. 109201.
- [47] T. Elfouhaily, B. Chapron, K. Katsaros, and D. Vandemark, "A unified directional spectrum for long and short wind-driven waves," *J. Geophys. Res.*, vol. 102, no. C7, Jul. 1997, Art. no. 15781.
- [48] W. Z. Shao, X. F. Li, P. Hwang, B. Zhang, and X. F. Yang, "Bridging the gap between cyclone wind and wave by C-band SAR measurements," *J. Geophysical Res., Oceans*, vol. 122, no. 8, pp. 6714–6724, Aug. 2017.
- [49] R. D. Viana, J. A. Lorenzetti, J. T. Carvalho, and F. Nunziata, "Estimating energy dissipation rate from breaking waves using polarimetric SAR images," *Sensors*, vol. 20, no. 22, Nov. 2020, Art. no. 6540.



Yuqi Hu received the B.S. and master's degrees in marine science from Zhejiang Ocean University, Zhoushan, China, in 2017 and 2021, respectively, and the Ph.D. degree in physical oceanography from Shanghai Ocean University (SHOU), Shanghai, China, in 2024.

Since July 2024, he has been a Postdoctor with SHOU. His major research interests include wave retrieval from SAR and wave simulation based on the numeric model.



Maurizio Migliaccio (Fellow, IEEE) was born in Naples, Italy, in 1962. He received the Laurea (Hons.) degree in electronic engineering from the Università degli Studi di Naples Federico II, Naples, Italy, in 1987.

Since 1994, he has been teaching microwave remote sensing. Since 2005, he has been a Full Professor of electromagnetics with the Università degli Studi di Naples Parthenope, Naples. Since 2013, he has been an Affiliated Full Professor with NOVA Southeastern University, Fort Lauderdale, FL, USA. He has authored or coauthored more than 200 peer-reviewed journal articles on remote sensing and applied electromagnetics. His research interests include applied electromagnetics.

Mr. Migliaccio was a Member of the Italian Space Agency Scientific Committee. He is an Associate Editor for the *International Journal of Remote Sensing* and *IEEE TRANSACTIONS ON GEOSCIENCES AND REMOTE SENSING*.



Armando Marino (Member, IEEE) received the M.Sc. degree in telecommunication engineering from the Università di Napoli "Federico II," Naples, Naples, Italy, in 2006, and the Ph.D. degree in polarimetric SAR interferometry from the School of Geosciences, University of Edinburgh, Edinburgh, U.K., in 2011.

In 2006, he joined the High Frequency and Radar Systems Department, German Aerospace Centre, Oberpfaffenhofen, Germany, where he developed his M.S. thesis. In 2011, he was with the University of Alicante, Institute of Computing Research, Madrid, Spain. From 2011 to 2015, he was a Postdoctoral Researcher and Lecturer with the Institute of Environmental Engineering, ETH Zurich, Zurich, Switzerland. In 2015, he was a Lecturer with the School of Engineering and Innovation, Open University, Milton Keynes, U.K. Since 2018, he has been an Associate Professor with the Faculty of Natural Sciences, University of Stirling, Stirling, U.K.



Weizeng Shao (Member, IEEE) received the B.S. degree in engineering from the Jiangsu University of Science and Technology, Zhenjiang, China, in 2007, and the Ph.D. degree in physical oceanography from the Ocean University of China, Qingdao, China, in 2013.

During his Ph.D. program in 2010–2012, he was a Visiting Research Scientist with the SAR oceanography group with the German Aerospace Center (DLR), Munich, Germany. In 2015–2020, he was an Associate Professor and master's student supervisor with

Zhejiang Ocean University, Zhoushan, China, and since 2019, he has been an Assistant Researcher with the National Satellite Ocean Application Service, Beijing, China. He has also been a Full Professor with Shanghai Ocean University, Shanghai, China, since 2021. His research interests include marine applications during tropical cyclone by synthetic aperture radar, especially from Chinese Gaofen-3 (GF-3), HY-2, 1mC-SAR, and CFOSAT, and ocean modeling of tropical cyclone by couple numeric models.



Xingwei Jiang received the Ph.D. degree in physical oceanography from the Ocean University of China, Qingdao, China, in 2008.

He became an Academician with the Chinese Academy of Engineering and a Doctoral Supervisor. He is currently the Director of the Chinese National Satellite Marine Application Center, Beijing, China, and the Chief Designer of the Chinese Marine Satellite Ground Application Systems. He presided over the establishment of a marine satellite ground application system platform and formulated marine remote

sensing technical regulations. He has published several monographs, atlases, and papers and formed a marine satellite ground application engineering technical team.

Dr. Jiang was the Vice Chairman of the Chinese Ocean Society and the China Association for Remote Sensing Applications. He was the Chairman of the Ocean Remote Sensing Professional Committee, Chinese Ocean Society and was a member of the international GEO Organization technical coordination group and the Sino-French marine satellite joint steering committee.